# Coastal Boundary Conditions and the Baroclinic Structure of Wind-Driven Continental Shelf Currents*

R. M. SAMELSON

*Woods Hole Oceanographic Institution, Woods Hole, Massachusetts*

## ABSTRACT

The generation of continental shelf currents by wind forcing is investigated by analytical and numerical methods. The investigation is motivated by observations from the Coastal Ocean Dynamics Experiment. A central assumption is that the vertical structure of the response over the inshore half of the shelf is controlled by the vertical distribution of the turbulent stress. This suggests a two-layer model of the wind-driven circulation, in which the upper layer represents a surface wind-mixed layer, and the lower layer represents the remainder of the fluid. The response of this idealized dynamical model to wind forcing is examined and compared with observations in the 2–7-day period band. For the alongshore velocity gain relative to local wind stress, an onshore surface maximum and an offshore interior maximum are robustly reproduced by the model. These features are evidently related to a dynamical transition over the inner half of the shelf, in which the alongshore wind stress is balanced more by acceleration of near-surface alongshore flow and less by time-dependent Ekman transport as the coast is approached. This differs from a previous hypothesis, based on a linear model in which the turbulent stress was confined to infinitesimally thin surface and bottom boundary layers, which related the alongshore flow structure to the cross-shore profile of the alongshore wind amplitude. In the present model, the cross-shore velocity variances are roughly comparable to those observed over the onshore half of the shelf. This also contrasts with the previous model results, which underpredicted cross-shore velocity variances by more than an order of magnitude. However, the present agreement is probably fortuitous, as the enhanced lower-layer cross-shore flow is frictionally driven, and should probably be confined to a bottom boundary layer as it was in the previous model. The results demonstrate that the response of these models over the inner half of the shelf depends strongly on a poorly understood coastal boundary condition.

## 1. Introduction

The coastal ocean is a complex fluid dynamical regime. Over the deeper continental shelf and slope, turbulence generated near the sea surface and sea floor is generally confined to boundary layers that are thin relative to the fluid depth. As the coastal boundary is approached, the fluid depth decreases until it is comparable to the penetration depth of surface and bottom boundary effects. Eventually, in the intrinsically nonlinear surf zone, the flow dynamics may be entirely dominated by small-scale three-dimensional motions, including turbulent and wave stresses and surface gravity wave breaking. The development and analysis of dynamical models of coastal circulation that explicitly represent the coupling of small-scale turbulence with the larger-scale near-geostrophic motion is at an early stage (e.g., Allen et al. 1995; Federiuk and Allen 1995). The parallel development and analysis of simplified models that provide conceptual insight is a necessary complement to this program. The present contribution is intended as part of the latter effort.

Despite the complexity of shelf flow fields, substantial quantitative success has been achieved in reproducing coastal sea level and alongshore velocity observations over the shelf and slope using linear coastal-trapped wave theory (Brink 1982, 1989; Allen and Denbo 1984; Battisti and Hickey 1984; Church et al. 1986; Chapman 1987). These calculations employ a small number of the gravest free linear long-wave coastal-trapped modes and a corresponding set of forced linear first-order wave equations for the evolution of the modal amplitudes (Gill and Schumann 1974; Huthnance 1975; Allen 1980; Brink 1991). The results emphasize the importance of remote forcing and alongshore wave propagation, although extensions to the theory have included locally forced, linear, short waves (Brink et al. 1987; Lopez and Clarke 1989). The quantitative success of coastal-trapped wave theory in reproducing a significant part of sea level and alongshelf velocity variability under many conditions has been dramatic (Brink 1991). However, Brink, et al. (1987) and

*Corresponding author address:* Dr. R. M. Samelson, Dept. of Physical Oceanography, Woods Hole Oceanographic Institution, Woods Hole, MA 02543.
E-mail: rsamelson@whoi.edu.

others have drawn attention to its equally dramatic failure to reproduce observations of cross-shore velocity and density fluctuations over the shelf.

In coastal-trapped wave theory, turbulent stresses are generally confined to infinitesimally thin boundary layers, while motion in the inviscid interior is controlled by the linear wave modes. This approach was followed, for example, in the model of Brink et al. (1987), the results of which provided some of the motivation for the present study. It contrasts with the point of view adopted in two-dimensional theories of coastal upwelling (de Szoeke and Richman 1984; Samelson and de Szoeke 1988), which focus on the dynamics of the surface boundary layer and include explicit representations of the upwelling and entrainment of interior fluid into the boundary layer. The present model attempts to combine the essential elements of these two approaches in the simplest possible way. In this regard, the present study can be seen as a continuation of the work of Brink et al. (1987), who noted that the absence of mixed layer physics might have contributed to the inability of their model to reproduce some aspects of the CODE observations.

The focus of the present study is the wind-driven circulation over the continental shelf on timescales of roughly 2–7 days. It is motivated primarily by observations from the Coastal Ocean Dynamics Experiment (CODE), which took place along the coast of northern California during 1981–82 (Winant et al. 1987). Statistical characteristics of the wind-driven shelf circulation in this frequency band are explored within the framework of a linear two-layer model, where the upper layer represents a surface wind-mixed layer, with a typical depth of 20 m, and the lower layer represents the remainder of the fluid, including the bottom boundary layer. The physical motivation for this choice of model consists primarily in the hypothesis that the vertical distribution of turbulent stress controls the vertical structure of horizontal motion over the shelf, so that an explicit representation of the wind-forced boundary layer

is necessary. An additional hypothesis is that the motion may be regarded as approximately adiabatic; that is, entrainment through the base of the wind-mixed layer is neglected. Note that the absence of interior baroclinity will result in errors in the structure and phase speeds of the coastal-trapped wave modes, and corresponding errors in certain features of the response. Similarly, errors will arise from the neglect of entrainment and horizontal advection of thickness and density in the surface boundary layer model. These errors are accepted here in order to obtain a minimal model that contains an explicit surface boundary layer but may be conveniently solved, in order to focus on the effect of the explicit surface boundary layer on the statistical characteristics of the response and to compare that response to CODE observations. As noted above, the attempt by Brink et al. (1987) to explain CODE observations in this frequency band (which contains an important fraction of the atmospheric forcing spectrum) with a dynamical model of the wind-driven circulation on the shelf was only partially successful. The present calculations suggest a possible alternative explanation of some details of the vertical and cross-shore structure of the alongshore velocity response. The results point to the sensitivity of the response over the inner half of the shelf to a poorly understood coastal boundary condition.

The model is outlined in section 2. The method for calculating of the linear response to stochastic forcing is reviewed in section 3. Section 4 contains the results, and section 5 a brief comparison with observations. The conclusions are summarized in section 6.

## 2. Model formulation

### a. Equations

The basic model has been motivated above. It consists of two homogeneous fluid layers of differing densities, separated by a material interface. The total depth of the fluid is variable. The linearized equations are

$$u_{1t} - f v_1 = -g \eta_x + (\tau_s^x - \tau_i^x)/H_1 \tag{2.1}$$

$$u_{1t} + f u_1 = -g \eta_y + (\tau_s^y - \tau_i^y)/H_1 \tag{2.2}$$

$$\zeta_t - H_1(u_{1x} + v_{1y}) = 0 \tag{2.3}$$

$$u_{2t} - f v_2 = -g \eta_x - g' \zeta_x + (\tau_i^x - \tau_b^x)/H_2 \tag{2.4}$$

$$v_{2t} + f u_2 = -g \eta_y - g' \zeta_y + (\tau_i^y - \tau_b^y)/H_2 \tag{2.5}$$

$$H_1(u_{1x} + v_{1y}) + u_2 H_{2x} + H_2(u_{2x} + v_{2y}) = 0 \tag{2.6}$$

$$H_1 + H_2(x) = D(x), \tag{2.7}$$

where $(u_j, v_j)$ are the $(x, y)$ components of horizontal velocity in layer $j$, $j = 1, 2$; $\zeta$ is the deviation of the internal interface from its resting depth $z = -H_1$; and $\tau_s^{(x,y)}$, $\tau_i^{(x,y)}$, $\tau_b^{(x,y)}$ are the kinematic surface, interfacial, and
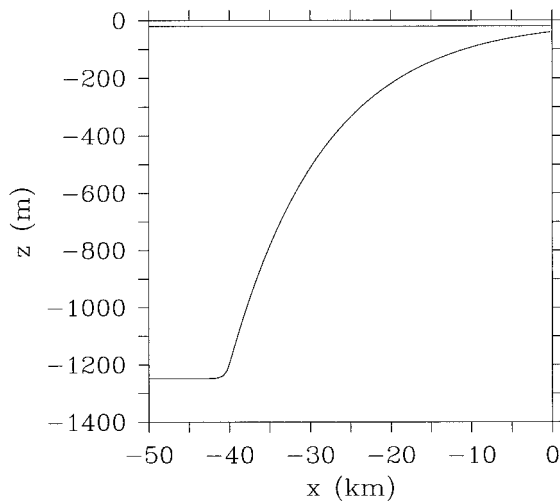
FIG. 1. Model geometry. The mean interface depth (20 m) and the exponential bottom depth profile are shown.

bottom stresses. The coordinate system is aligned so that the coastal boundary is at $x = 0$, $x$ decreases offshore, and $y$ increases northward. The rigid-lid approximation has been made, so the total fluid depth $D(x)$ is independent of time, and $\eta$ is an equivalent free-surface height associated with the surface pressure. The parameters $g$ and $g' = g\Delta\rho/\rho$ are the gravitational acceleration and the reduced gravity of the internal interface, respectively, where $\Delta\rho$ is the density difference between the layers and $\rho$ is a reference density. There is no entrainment of lower layer fluid into the upper layer. The bottom depth is taken to increase exponentially offshore (Fig. 1). The linear theory of the free waves that arise in this two-layer model with exponential topography has been developed by Allen (1975).

The upper layer represents the surface wind-mixed layer. Its mean thickness is a parameter that must be specified. Estimated vertical penetration depths of turbulent stress during CODE varied substantially over both space and time, and a single surface boundary layer depth scale could not be unambiguously extracted from the CODE observations (Davis and Bogden 1989). In the present calculations, the mean depth of the upper layer is taken to be 20 m. This choice is roughly consistent with the results of Lentz (1992), who found that the surface mixed layer depth during CODE varied between 0 and 20 m and that a surface flow quantitatively consistent with wind-driven Ekman transport dynamics was distributed between the surface mixed layer and a transition layer at the mixed layer base that was typically half as thick as the mixed layer. The qualitative results of the present calculations do not depend sensitively on the choice of 20-m mean depth for the wind-driven layer. The lower layer includes both the inviscid interior and the bottom boundary layer.

### b. Coastal boundary conditions

The coastal boundary conditions form an important part of any dynamical model of flow over the continental shelf. Mitchum and Clarke (1986) showed that for long waves, net cross-shore flow is effectively blocked when the total fluid depth reaches three times the Ekman layer thickness, and suggested on those grounds that a coastal boundary condition of no net cross-shore transport may be consistently applied at the offshore location where the total mean fluid depth reaches that value. However, in order to close the problem it is generally necessary also to specify a boundary condition on the depth-dependent flow. In coastal-trapped wave theory and its extensions, the second condition usually appears as a requirement that at the coastal boundary, the inviscid interior flow that balances the cross-shore transport in surface and bottom boundary layers itself be depth-independent at the coastal boundary (Brink et al. 1987; Clarke and Lopez 1987). The vertical motion that accompanies the surface Ekman transport divergence adjacent to the coast is presumed to occur in the inner shelf and nearshore regimes, shoreward of the model's "coastal" boundary and without explicit dynamical constraints. This condition can be motivated by scaling arguments if the stratification is sufficiently weak. In the following, these two conditions are together referred to as the "barotropic" coastal boundary conditions.

In the two-layer model, the most natural coastal boundary condition to apply is no normal flow in each layer (Allen 1975). That is, the depth-dependent flow is required to vanish along with the depth-independent flow. These no-normal-flow coastal boundary conditions,

$$u_1 = u_2 = 0 \quad \text{at} \quad x = 0, \qquad (2.8)$$

are adopted in the present study, and applied where the fluid depth reaches 40 m. In this case, the vertical motion induced by Ekman divergence near the coastal boundary is forced to occur within the model domain, and no flow is allowed to pass through the inner shelf and nearshore regimes.

The imposition of a coastal boundary condition in fluid of finite mean depth changes the basic geometry of the domain, by removing the shallow wedge-shaped nearshore and surf zone. Thus, it might be argued that in order to reproduce the main features of the depth-dependent flow, it would be necessary to solve the problem all the way up through the surf zone to the beach, where the fluid depth vanishes. Apart from the technical challenges that such an approach would entail, this seems an unreasonably severe requirement. As the coastal boundary is approached, the momentum injected at the surface by the wind is transferred to the bottom boundary with increasing efficiency, and the development of an offshore Ekman transport in a surface frictional layer is impeded, as the surface and bottom boundary layers merge. There is evidence from CODE

observations that turbulent (or wave) stresses penetrate the entire water column at depths as great as 60 m (Davis and Bogden 1989). CODE observations indicate that the cross-shore Ekman transport at the 30-m isobath is typically about one-tenth the midshelf transport (Lentz 1994), with about half of the reduction apparently arising from a linearly interpolated estimate of the onshore decrease in local wind over the inner shelf, and about half from a reduced Ekman reponse associated with the merging of the boundary layers. Thus, the imposition of a no-normal-flow condition at the 40-m isobath appears to be crudely consistent with some aspects of the CODE observations. In the CODE region, the topographic contours rise steeply inshore of the 50-m isobath, so the idealized vertical wall no-normal-flow condition may be particularly appropriate.

The boundary conditions (2.8) differ from the "barotropic" coastal boundary conditions in their effect on the momentum balance adjacent to the coastal boundary. When the conditions (2.8) are adopted, the alongshore wind stress imparted to the fluid adjacent to the coastal boundary is balanced in the surface layer by the alongshore pressure gradient, the acceleration of a geostrophic alongshore flow, and a small interfacial drag. Motion in the lower layer is driven only by interfacial drag and pressure gradients. Thus, the vertical distribution of turbulent stress directly influences the vertical structure of the flow near the wall, through the coastal boundary condition, since normal flow must vanish separately in each layer. In contrast, when the barotropic conditions are adopted, the alongshore wind stress is instead balanced by a depth-independent pressure gradient and acceleration of a depth-independent alongshore flow, and by bottom drag. In that case, the flow does not satisfy a no-normal-flow condition at the coastal boundary at any point in the water column. Instead, the vertical structure of the flow near the wall is fixed by the requirement that the interior flow at the wall be independent of depth, while the vertical motion accompanying inner-shelf Ekman divergence occurs outside the model domain, without any explicit dynamical constraints. Because of this fundamental difference in boundary condition, the continuously stratified Brink et al. (1987) model does not reduce to the present model in the limit of a corresponding two-layer density profile. In order to focus on the effect of the different boundary conditions and exclude complications that arise from other differences between the two models, the present results are compared below with results obtained from the present model with barotropic boundary conditions similar to those used by Brink et al. (1987).

## 3. Formulation and method of solution

In this section, the linear response of the present model to stochastic forcing is computed following the method of Brink et al. (1987). The results and parameters will be presented in dimensional form, for ease of comparison with observational estimates of the predicted statistical quantities. Since the dominant energy in the forcing field is in the alongshore component (e.g., Brink et al. 1987), only alongshore wind-forcing

$$T(x, y, t) = \tau^y(x, y, t) \tag{3.1}$$

is considered (so $\tau^x = 0$). The interfacial and bottom stresses are represented by linear drag,

$$(\tau_i^x, \tau_i^y) = R_i(u_1 - u_2, v_1 - v_2),$$
$$(\tau_b^x, \tau_b^y) = R_b(u_2, v_2), \tag{3.2}$$

with $R_i = 4 \times 10^{-5}$ m s$^{-1}$, $R_b = 4 \times 10^{-4}$ m s$^{-1}$. The latter value for $R_b$ is the constant value used by Brink et al. (1987) in the absence of wave stress effects and is used here for consistency since attention is here restricted to the case of constant frictional coefficients. The value of $R_i$ is chosen to be one order of magnitude smaller than $R_b$. The bottom topography is taken to be independent of $y$,

$$D(x) = D(0)e^{x/\lambda}, \qquad x_a \leq x < 0 \tag{3.3}$$

$$D(x) = D(x_a) + \Delta D_a(1 - e^{(x-x_a)/\lambda_a}),$$
$$x_1 < x < x_a, \tag{3.4}$$

where $D(0) = 40$ m, $\lambda = 0.85 \times 10^{-4}$ m$^{-1}$, $x_a = -40$ km, $x_1 = -50$ km is the offshore boundary of the computational domain, $\Delta D_a = 50$ m, and $\lambda_a$ is chosen to make the first derivative of $D$ continuous at $x = x_a$. This gives a maximum depth of approximately 1250 m (Fig. 1). Some of the computations were repeated with $x_a = -50$ km and $x_1 = -60$ km, giving a maximum depth of approximately 2850 m; this led to no significant changes in the qualitative or quantitative results over the inner half of the shelf ($-15$ km $< x < 0$).

Solutions are obtained by Fourier transform in $y$ and $t$, denoted by

$$\hat{u}_j = \mathcal{F}[u_j], \qquad \hat{v}_j = \mathcal{F}[v_j], \qquad j = 1, 2; \qquad \hat{\zeta} = \mathcal{F}[\zeta], \tag{3.5}$$

where the Fourier transform $\mathcal{F}[\phi]$ of a function $\phi$ is defined by

$$\mathcal{F}[\phi] = \int\int \phi e^{i(ly+\omega t)} \, dy \, dt. \tag{3.6}$$

This yields two coupled second-order linear ordinary differential equations in $x$, which are solved numerically by standard finite-difference methods. Boundary conditions of exponential decay offshore are employed at $x_1$ using the flat-bottom analytic solutions in a manner similar to that of Allen (1975).

The Fourier transform solution for a dependent variable $X$ may be written formally as

$$\hat{X}(x, l, \omega) = B_X(x, l, \omega)\hat{T}(x, l, \omega), \tag{3.7}$$

where $B_X$ is the transfer function for the variable $X$ that results from the solution of the linear differential equations in $x$. The ensemble-averaged cross-spectrum $S_{XT}$

of a dependent variable $X(x, y, t)$ and the local forcing $T(x, y, t)$ at the frequency $\omega$ may be expressed in terms of the Fourier transform solutions,

$$S_{XT}(x, \omega) = \frac{1}{2\pi} \int \{\hat{X}(x, l, \omega)\overline{\hat{T}}(x, l, \omega)\} \, dl \quad (3.8)$$

$$= \frac{1}{2\pi} \int B_X(x, l, \omega)\{\hat{T}(x, l, \omega)\overline{\hat{T}}(x, l, \omega)\} \, dl, \quad (3.9)$$

where an overbar denotes complex conjugate and braces denote the ensemble average. Similarly, the power spectrum $S_{XX}$ at the frequency $\omega$ is

$$S_{XX}(x, \omega) = \frac{1}{2\pi} \int \{\hat{X}(x, l, \omega)\overline{\hat{T}}(x, l, \omega)\} \, dl \quad (3.10)$$

$$= \frac{1}{2\pi} \int B_X(x, l, \omega)\overline{B}_X(x, l, \omega)$$

$$\times \{\hat{T}(x, l, \omega)\overline{\hat{T}}(x, l, \omega)\} \, dl, \quad (3.11)$$

where $B_X = 1$ for $S_{TT}$. These integrals may be evaluated if the ensemble-averaged wavenumber–frequency power spectrum of the wind stress,

$$S_T(x, l, \omega) = \{\hat{T}(x, l, \omega)\overline{\hat{T}}(x, l, \omega)\}, \quad (3.12)$$

is specified. The simple form

$$S_T(x, l, \omega) = A(x, \omega)\frac{2s}{s^2 + l^2} \quad (3.13)$$

is used here. From comparison with the observational estimates of the wind-stress spectrum used by Brink et al. (1987), the constant value $s = 3.1 \times 10^{-6}$ m$^{-1}$ was chosen for the present calculations for all $\omega$, corresponding to a coherence decay scale of $s^{-1} = 320$ km. The results do not depend sensitively on the particular choice of $s$. In most of the calculations, the wind stress power spectrum $S_T$ is taken to be independent of the cross-shore coordinate $x$. The effect of alongshore variations in the amplitude of the wind stress has been explored by Brink et al. (1987) and is not considered here, in order to focus on the simplest case.

As in Brink et al. (1987), the solutions are presented in terms of the gain $R_{XT}$, coherence $\gamma_{XT}$, and phase $\theta_{XT}$, where

$$R_{XT}(x, \omega) = S_{XT}/S_T = \gamma_{XT}(S_X/S_T)^{1/2} \quad (3.14)$$

$$\gamma_{XT}(x, \omega) = \left(\frac{S_{XT}\overline{S}_{XT}}{S_X S_T}\right)^{1/2} \quad (3.15)$$

$$\theta_{XT}(x, \omega) = \arg[S_{XT}]. \quad (3.16)$$

## 4. Results

### a. Gain, coherence, and phase

#### 1) STANDARD CASE

In this section, the model response to stochastic forcing is examined for forcing frequencies in the range $10^{-6}$ s$^{-1} < \omega < 6 \times 10^{-5}$ s$^{-1}$, corresponding to periods between 72 and 1.2 days. The central focus is on frequencies in the range $10^{-5}$ s$^{-1} < \omega < 3 \times 10^{-5}$ s$^{-1}$, corresponding to periods between 7 and 2.4 days. In this range, comparisons will be made below with the estimates by Brink et al. (1987) of statistical quantities from CODE observations. The results shown here are for the case in which the fractional change in density across the mixed layer base is $\Delta\rho/\rho = 0.25 \times 10^{-3}$. The qualitative results are not sensitive to this value.

The surface-layer and lower-layer alongshore velocity gain, $R_{v_1 T}$ and $R_{v_2 T}$, respectively, are shown versus frequency and cross-shore distance in Fig. 2. The surface-layer and lower-layer gains differ in structure. The surface-layer gain $R_{v_1 T}$ increases onshore and toward low frequency, and also weakly offshore and toward high frequency, with an intermediate minimum that moves onshore across the shelf toward high frequency. The lower-layer alongshore velocity gain $R_{v_2 T}$ also increases toward low frequency but has a single maximum at each frequency, located roughly 5-km offshore at all frequencies. This maximum is most prominent at low frequencies. The structure of the alongshore velocity response on the inner half of the shelf is interpreted below in terms of the baroclinic modifications of barotropic continental shelf waves described for the two-layer model by Allen (1975). The location of the offshore maximum in alongshore velocity gain depends on the local internal deformation radius $L_D = (g'H_1/2)^{1/2}/f = 2.2$ km, which controls the width of the baroclinic zone adjacent to the coast. There is a maximum at a similar location in the lower-layer cross-shore velocity gain $R_{u_2 T}$ (Fig. 2d), which increases slowly toward increasing frequency. The surface-layer cross-shore velocity gain $R_{u_1 T}$ increases rapidly offshore over the first 5–10 km and is nearly uniform farther offshore, increasing weakly toward high frequency (Fig. 2c). The interface displacement gain $R_{\zeta T}$ increases uniformly onshore (Fig. 2e). It is relatively independent of frequency, with a rapid increase only over the very lowest frequencies considered, $\omega < 0.5 \times 10^{-5}$ s$^{-1}$. The surface pressure (equivalent sea surface height) gain increases onshore and toward low frequency (Fig. 2f).

The coherence $\gamma_{v_1 T}$ of alongshore velocity in the surface layer and alongshore wind stress has two maxima, one offshore and one onshore, and both maxima increase toward high frequency (Fig. 3a). The offshore maximum covers most of the shelf at the highest frequencies, and almost none of it at the lowest frequencies. The high-frequency offshore regime is evidently characterized by the dominance of alongshore over cross-shore gradients. If all $x$-derivatives are neglected in (2.1)–(2.6), the resulting solution for a single Fourier component of forcing has amplitude and phase (see below) structure consistent with these results; it asssumes flat-bottom topography and does not satisfy the coastal boundary conditions (2.8), so that it can only be relevant sufficiently far offshore. The intermediate minimum roughly over-
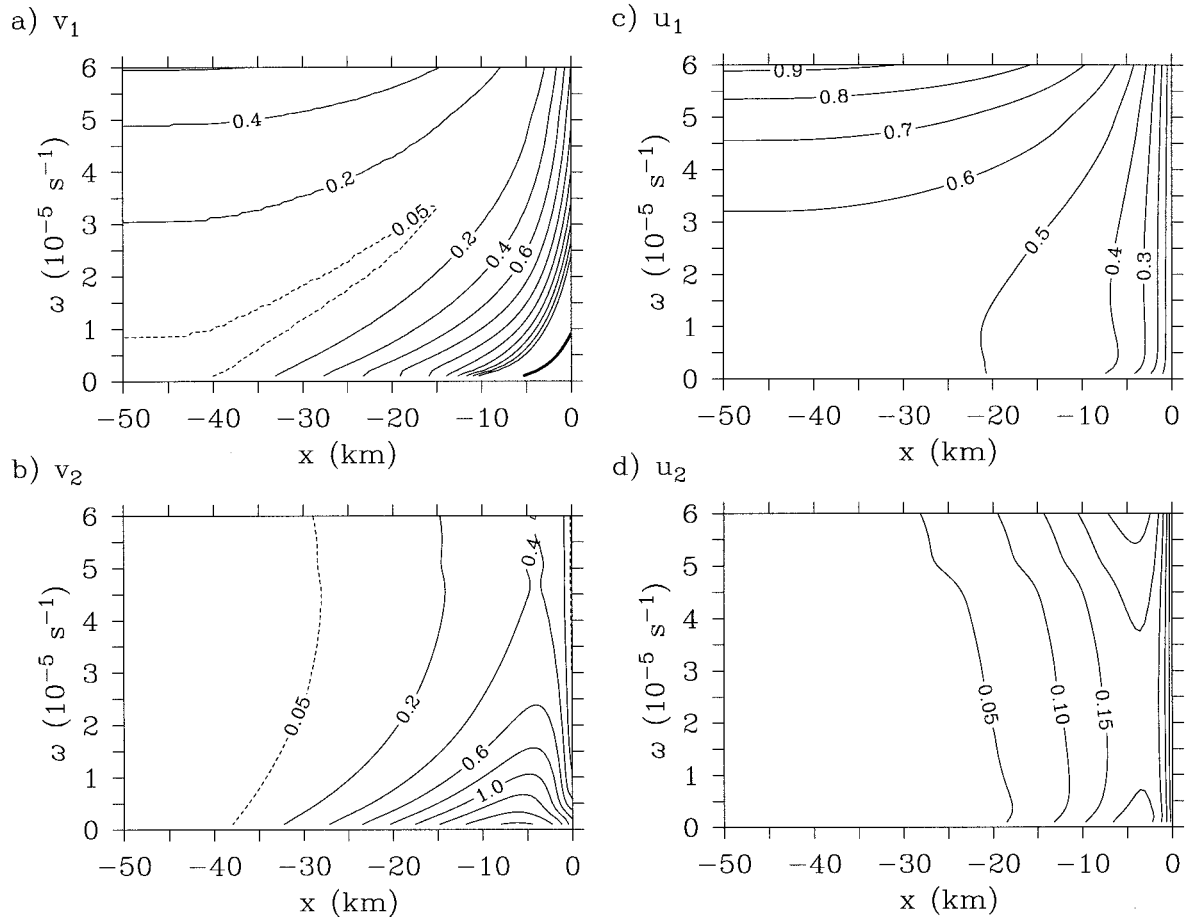
FIG. 2. Contours of gain vs frequency $\omega$ and offshore distance $x$ for the case with exponential topography and no-normal-flow boundary conditions in each layer: (a) $R_{v_1 T}$, (b) $R_{v_2 T}$, (c) $R_{u_1 T}$, (d) $R_{u_2 T}$, (e) $R_{\zeta T}$, and (f) $R_{\eta T}$. The units are m$^2$ s$^{-2}$/(N m$^{-2}$)$^2$ in (a)–(d) and m$^2$/(N m$^{-2}$)$^2$ in (e),(f). In (a), the thick line is the 5 contour, and no other contours greater than 2 are shown. In (e), the unlabeled contours are 100, 200, 500, and 1000. In (f), the contour interval is 0.05, and the contours at the lower right increase monotonically from 0.05.

lays on the gain minimum. The coherence $\gamma_{v_2 T}$ of lower-layer alongshore velocity and alongshore wind stress increases more uniformly toward high frequency, with a relative maximum that overlays roughly on the interior gain maximum at low frequency, and a maximum over the steepest bottom slopes for intermediate frequencies (Fig. 3b). The coherence $\gamma_{v_1 T}$ of cross-shore surface-layer velocity and alongshore wind stress is uniformly large (not shown). The coherence $\gamma_{u_2 T}$ of lower-layer cross-shore velocity and alongshore wind-stress is uniformly large at high frequencies but degrades rapidly offshore at intermediate and lower frequencies (Fig. 3c). The coherence $\gamma_{\zeta T}$ of interface displacement and alongshore wind stress is relatively independent of frequency. It is large near the coast and decreases rapidly offshore (Fig. 3d).

For alongshore velocity in the surface layer, a positive response lags the alongshore wind stress by a quarter period near the coast, while a negative response lags the wind stress by a quarter period offshore (Fig. 4a). The phase changes rapidly across the minimum in gain

and coherence. The lower-layer alongshore velocity lags the wind stress everywhere over the shelf, with the lag increasing toward high frequency (Fig. 4b). The phase decreases rapidly at the base of the sloping topography. As noted above, the phase structure of the high-frequency offshore response is consistent with a transition offshore to an $x$-independent flat-bottom dynamical regime, in which the interface displacement (not shown) is dominated by convergence of the alongshore flow. The cross-shore velocity in the surface layer is essentially in phase with the wind forcing everywhere (offshore flow for southward wind stress) since it is dominated by the time-dependent Ekman balance. The lower-layer cross-shore velocity is out of phase with the wind forcing everywhere (onshore flow for southward wind stress), as would be required to balance the offshore flow in the surface layer if the transport balance were two-dimensional (Fig. 4c). A negative interface displacement (consistent with downwelling for northward wind stress) lags the wind stress by roughly a quarter period (Fig. 4d). Thus, over the inner half of
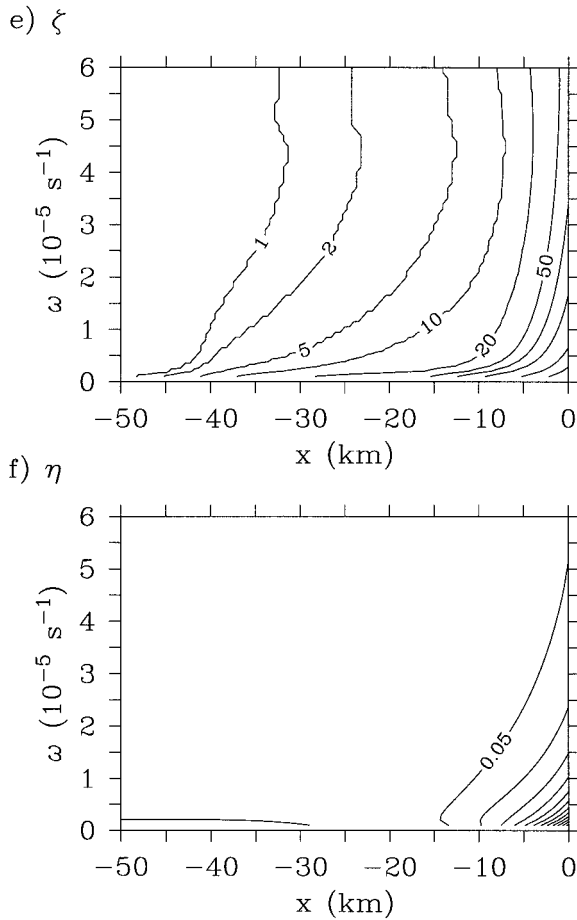
e) $\zeta$



f) $\eta$



Fig. 2. (*Continued*)

the shelf the interface displacement is out of phase with the alongshore velocities, consistent with an approximate geostrophic balance of the alongshore flow for which an interface rising toward the coast corresponds to southward geostrophic flow in the surface layer.

2) DEPENDENCE ON FRICTION

The qualitative results are relatively insensitive to the values of the bottom and interfacial frictional coefficients. The quantitative results do depend on these values. If the friction coefficients are doubled, the offshore maximum in lower-layer alongshore velocity gain $R_{v_2T}$ decreases from 1 to 0.8 (units as in Fig. 2) for $\omega = 10^{-5}$ s$^{-1}$, while the offshore maximum in lower-layer cross-shore velocity gain $R_{u_2T}$ increases from 0.19 to 0.23. If the friction coefficients are reduced by half, these maxima respectively increase from 1 to 1.2 and decrease from 0.19 to 0.17.

3) DEPENDENCE ON CROSS-SHORE WIND-STRESS PROFILE

The results shown here were obtained with wind stress independent of cross-shore distance. Results were

also obtained with the amplitude of the wind stress decreasing linearly toward the coast over an 8-km region adjacent to the coast as in Brink et al. (1987), with the coastal minimum equal to one-third the offshore value, so that the effective wind stress curl was partially distributed over the 8-km region instead of entirely concentrated at the coastal boundary. In this case, the statistical quantities at each location were computed using the constant offshore wind stress amplitude for normalization. The offshore maxima in $R_{v_2T}$ and $R_{u_2T}$ both decreased, the former from 1 to 0.8 (units as in Fig. 2) and the latter from 0.19 to 0.13 for $\omega = 10^{-5}$ s$^{-1}$, and shifted several kilometers offshore, but the qualitative character of the lower-layer response was unchanged. The surface-layer responses changed more dramatically, with the alongshore velocity gain $R_{v_1T}$ developing a second local maximum offshore (at $x = -8$ km) equal in magnitude to the persisting coastal maximum, and the cross-shore velocity gain $R_{u_1T}$ decreasing by half. The offshore temperature response was enhanced by the local response to the wind stress curl, but this effect was essentially confined to the 8-km region adjacent to the coast.

4) DEPENDENCE ON COASTAL BOUNDARY CONDITION

The effect of the coastal boundary condition on the velocity response may be directly illustrated by recalculating the present solutions with barotropic boundary conditions similar to those employed by Brink et al. (1987). The first, no net normal flow at the coastal boundary, is easily implemented:

$$H_1u_1 + H_2u_2 = 0 \quad \text{at} \quad x = 0. \quad (4.1)$$

The second condition is that the pressure gradient that appears in the dynamical balance associated with the no-normal-flow condition be depth-independent in order that the vertical integral of the pressure gradient may be evaluated by multiplying the pressure gradient by the local fluid depth. In the present model, there is some ambiguity in formulating a corresponding condition, since the lower-layer flow includes the bottom Ekman layer. The condition used here is

$$(i\omega + R_i/H_2 + R_b/H_2)\zeta_x + f\zeta_y = 0 \quad \text{at} \quad x = 0, \quad (4.2)$$

which effectively prevents the forcing of cross-shore flow in the lower layer by internal pressure gradients associated with deformation of the interface.

The alongshore and cross-shore velocity gains that obtain with the boundary conditions (4.1) and (4.2), and other parameters as in the basic case, are shown in Fig. 5. The alongshore velocity response is essentially independent of depth over most of the shelf, and the previous offshore gain maximum in the lower layer has been replaced by a gain that increases monotonically onshore. Similarly, the cross-shore velocity gain in the
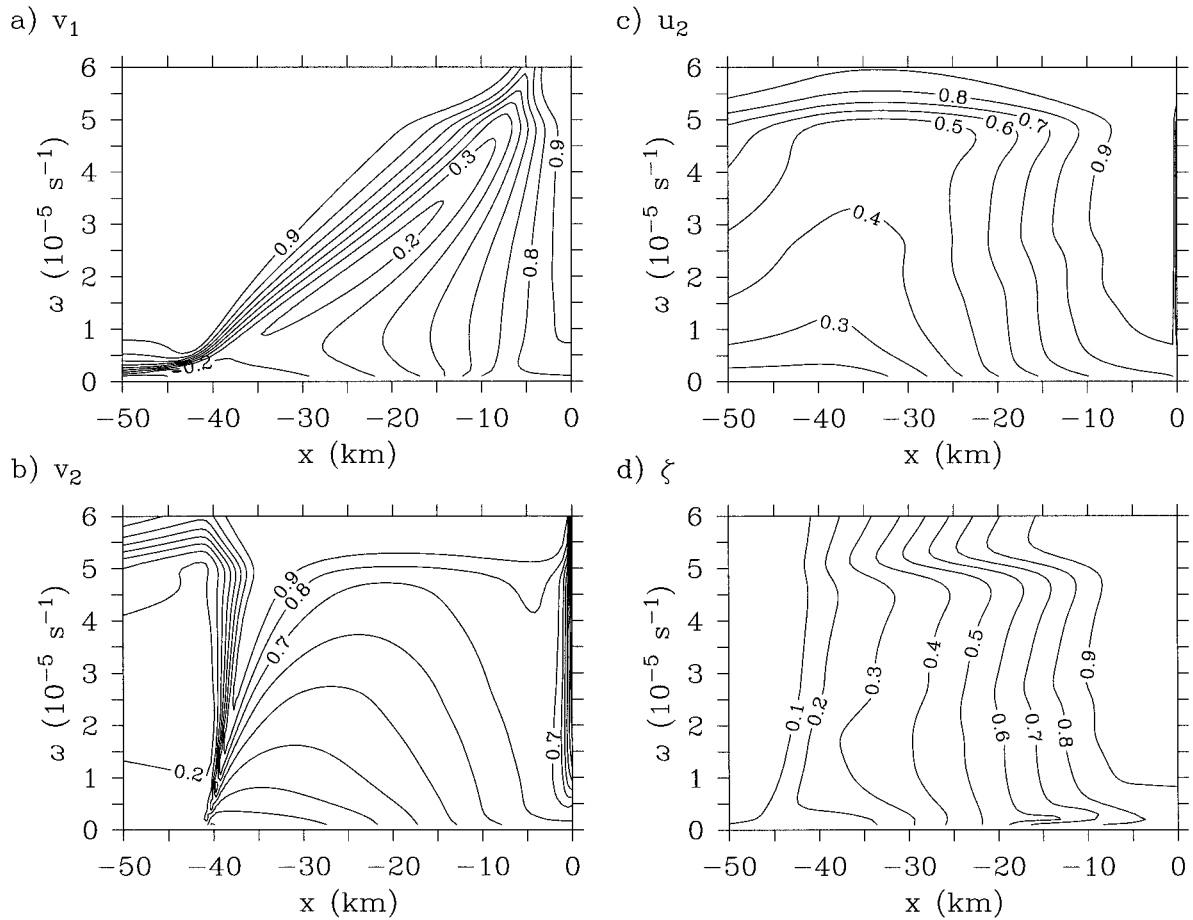
a) $v_1$

c) $u_2$

b) $v_2$

d) $\zeta$

FIG. 3. Contours of coherence vs frequency $\omega$ and offshore distance $x$ for the case shown in Fig. 2: (a) $\gamma_{v_1 T}$, (b) $\gamma_{v_2 T}$, (c) $\gamma_{u_2 T}$, and (d) $\gamma_{\zeta T}$.

lower layer now increases monotonically onshore. The maximum cross-shore velocity gain at the coast is larger than the previous offshore maximum, while the gain at the location of the previous offshore maximum has nearly the same value that it had previously at that location, despite the change in qualitative structure. These results will be discussed further below.

The baroclinic adjustment zone that appears adjacent to the coast in the solutions with the no-normal-flow conditions (2.8) will become arbitrarily narrow if the stratification becomes sufficiently weak. In that limit, the barotropic conditions (4.1) and (4.2) can be consistently applied, as the baroclinic zone has a boundary-layer character. In Allen's (1975) analysis of free waves in the two-layer model, boundary-layer methods are used explicitly to obtain solutions in the coastal baroclinic zone.

5) DEPENDENCE ON BOTTOM TOPOGRAPHY

The two calculations above may be contrasted with the response that obtains when the sloping topography is replaced by a flat bottom, so that the fluid has a uniform depth of 40 m, and the no-normal-flow con-

ditions (2.8) are again applied in each layer at the coastal boundary. In that case, the only remaining trapped wave mode is the Kelvin wave, which at the frequencies considered has a wavelength much shorter than the dominant alongshore scales of the wind forcing; consequently the statistics are controlled by the off-resonant response to the dominant large-scale forcing. The alongshore velocity and interface displacement gains are large only within 5 km of the coast, and the lower-layer alongshore velocity gain does not have an offshore maximum. The cross-shore velocity gains are nearly uniform, except adjacent to the coast. The interface displacement gain is tightly trapped to the coast, and the surface pressure is essentially independent of cross-shore distance. The alongshore velocity coherences have a minimum 5–10 km offshore. This minimum evidently indicates a transition to flow dominated by alongshore gradients, as occurs farther offshore and at high frequencies for the exponential topography. The coherence offshore increases with increasing frequency, while adjacent to the coast the coherence is uniformly high. The lower-layer cross-shore velocity coherence is uniformly high everywhere, while the interface displacement coherence
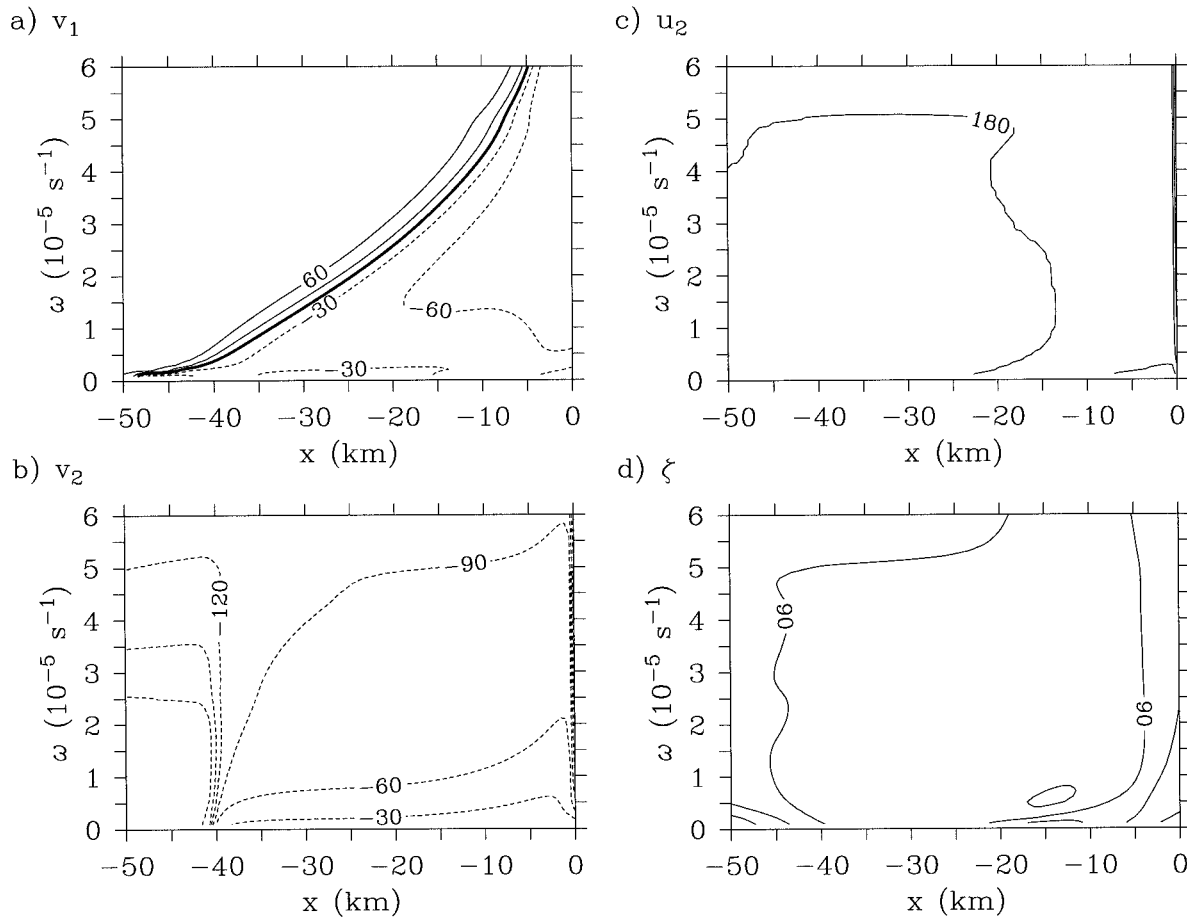
FIG. 4. Contours of phase (in degrees, contour interval 30°) vs frequency $\omega$ and offshore distance $x$ for the case shown in Fig. 2: (a) $\theta_{v_1T}$, (b) $\theta_{v_2T}$, (c) $\theta_{u_2T}$, and (d) $\theta_{\zeta T}$.

is large only adjacent to the coast where the interface displacement gain is also large.

The most striking qualitative difference between the sloping bottom and flat-bottom results is the structure of the alongshore velocity gain. In the former case, the lower-layer gain has a pronounced maximum 5 km offshore, while in the latter the maximum occurs at the coast and there is rapid decay offshore. The offshore decay scale is generally greater for all variables in the sloping bottom case. With the sloping bottom, the alongshore velocity gains in both layers are roughly twice as large as for the flat bottom. In contrast, the interface displacement gain is greater by only half with the sloping bottom.

### b. Transfer functions

The statistical characteristics of the linear response discussed above may be interpreted in terms of linear free waves by examining the structure of the transfer functions $B_X(x, l, w)$. Two shelf wave resonances and the internal Kelvin wave resonance are evident in the upper-layer alongshore velocity transfer function at off-

shore distance $x = -5$ km (Fig. 6). These resonances may be readily identified by comparing Fig. 6 with the qualitative features of the dispersion relation shown in Fig. 5 of Allen (1975). The shelf waves are supported by the bottom slope, while the internal Kelvin wave depends on the interior interface meeting the vertical coastal boundary. For $\omega \approx 10^{-5}$ s$^{-1}$, the Kelvin wave has $l \approx 6 \times 10^{-5}$ m$^{-1}$, and the shelf waves have $l_1, l_2 \approx 0.5, 3 \times 10^{-5}$ m$^{-1}$ (Fig. 6). The longer shelf wave resonance ($l \approx 0.5 \times 10^{-5}$ m$^{-1}$) dominates the linear response, because of the large scales of the wind forcing.

These resonances may also be distinguished, though less clearly, in contour plots of the cross-shore structure of the transfer function amplitudes for $\omega \approx 10^{-5}$s$^{-1}$ (Fig. 7). At the first shelf wave resonance, the offshore structure of the alongshore velocity transfer function is nearly identical in the upper and lower layers, as the barotropic shelf wave dynamics dominate (Figs. 7a,b). Adjacent to the coastal boundary, however, the upper-layer response increases onshore while the lower-layer response decreases. Since the transfer functions for given $l$ depend both on the free wave resonances and the cross-shore spatial structure of the forcing, this must be understood
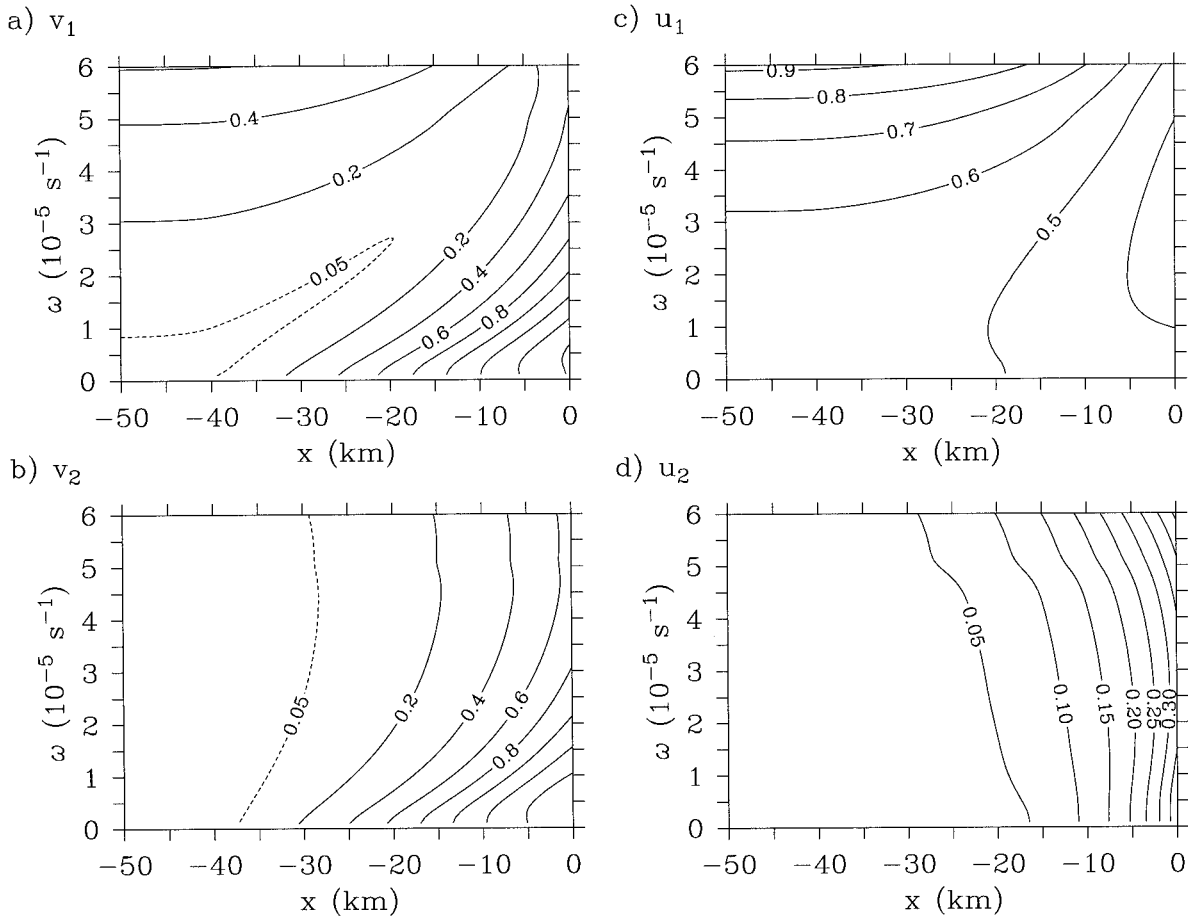
FIG. 5. Contours of gain vs frequency $\omega$ and offshore distance $x$ for the case with exponential topography and the barotropic boundary conditions (4.1) and (4.2): (a) $R_{v_1T}$, (b) $R_{v_2T}$, (c) $R_{u_1T}$, (d) $R_{u_2T}$, (e) $R_{\zeta T}$, and (f) $R_{\eta T}$. In (a), (b), and (f), the contours at the lower right increase monotonically, with fixed contour interval. Units are as in Fig. 2.

as a consequence both of the momentum balance at the coastal boundary discussed above (section 2b) and the coastal-trapped baroclinic (Kelvin wave) modification of the barotropic shelf wave in the two-layer model discussed by Allen (1975). That is, the momentum injected into the surface layer by the wind stress is trapped in the surface layer near the coast; this locally forced baroclinic response resembles an internal Kelvin wave, but is resonant at the shelf wave frequency, since it is an intrinsic part of the free shelf wave in the two-layer model. The baroclinic modification of the free shelf wave arises from interface displacements at the coastal boundary that are generated by barotropic motion across the sloping bottom. The coupling is governed by the ratio $L_D/\lambda$ of the coastal internal deformation radius to the topographic length scale (Allen 1975). For the parameters chosen here, $L_D/\lambda = 0.2$.

Within 10 km of the coast, the surface-layer cross-shore velocity transfer function is smaller for resonant and near-resonant wavenumbers than for off-resonant wavenumbers (Fig. 7c). Presumably, this decrease near resonance reflects a reduction in the cross-shore Ekman

transport that results when the wind stress preferentially accelerates the resonant alongshore flow. In contrast, the lower-layer cross-shore velocity transfer function is enhanced roughly 5 km offshore at each resonance, though it always drops to zero at the coast as a consequence of the no-normal-flow condition (Fig. 7d). This suggests that some of the cross-shore velocity response might be associated with the coastal-trapped baroclinic (Kelvin wave) modifications to the resonant shelf waves, rather than with the return flow balancing the cross-shore Ekman transport. This would be important because the results of Brink et al. (1987) suggest that the return flow should be confined to the bottom boundary layer at these frequencies, rather than being distributed over the interior as in the present model.

Since the model is linear, the lower-layer velocities may be split into an inviscid, inertial "interior" response to the pressure gradient and a viscous and inertial remainder that is driven by the the frictional stress from the interior component and may be interpreted as a "bottom Ekman layer" component. The cross-shore velocity gains for the interior component defined in this manner
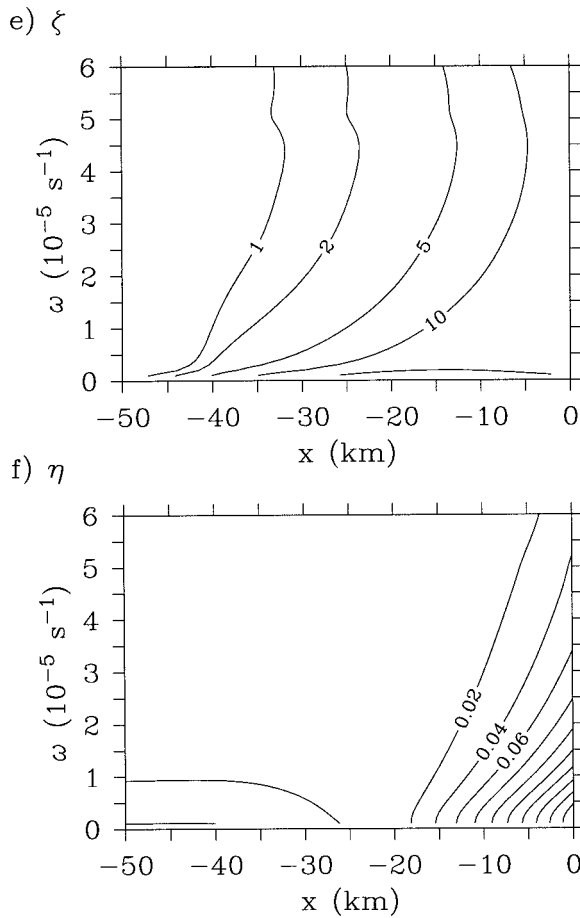
e) ζ



f) η



FIG. 5. (*Continued*)



FIG. 6. Contours of transfer function amplitude $(B_X \overline{B}_X)^{1/2}$ for variable $X = v_1$ vs frequency $\omega$ and alongshore wavenumber $l$ at offshore distance $x = -5$ km. The short-dashed line shows the wavenumber dependence of the wind stress power spectrum (on a linear scale, with arbitrary maximum amplitude) $S_T$. The long-dashed line indicates the frequency $\omega = 1.08 \times 10^{-5}$ s$^{-1}$, for which the cross-shore structure of the transfer function amplitudes are shown in Fig. 7.

are small (Fig. 8). Thus, the relatively large lower-layer cross-shore velocity response noted above (Figs. 2d, 5d, 7d) reflect frictionally driven transport that is combined with the inviscid interior response in the two-layer model. This is consistent with the small interior cross-shore velocity response found by Brink et al. (1987). Since the cross-shore velocities are primarily driven by the bottom stress from the alongshore flow, the structure of the cross-shore velocity response resembles that of the alongshore response, with an offshore maximum for the no-normal-flow coastal boundary conditions (Figs. 2b,d) and a monotonic onshore increase for the barotropic conditions (Figs. 5b,d). For the no-normal-flow conditions, the lifting of the interface adjacent to the coast is partially supported in the lower layer by a convergence of the frictionally driven transport distributed over the baroclinic zone adjacent to the coast.

The velocity response associated with the shelf wave resonance extends across most of the shelf. In contrast, the shelf wave resonances are nearly indiscernible in the interface displacement transfer function (Fig. 7e). This is consistent with the weaker dependence on topography of the interface displacement response, relative to the velocity response: The absence of the shelf
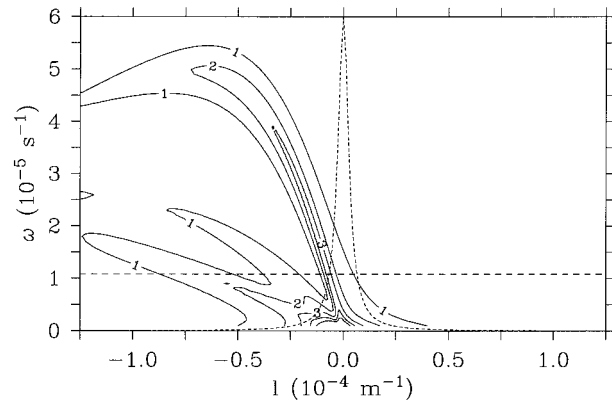
wave in the case with flat-bottom topography has little effect on the amplitude of the interface displacement, apparently because that displacement is dominated by the off-resonant response (near the zero-wavelength maximum of the wind stress spectrum) to Ekman divergence, rather than by the resonant shelf-wave response. (The Kelvin wave resonance itself is clearly evident in the interface displacement transfer function but is located at sufficiently large wavenumber that the corresponding amplitude of the wind stress forcing is negligible.) The alongshore velocity response is apparently dominated to a greater degree by resonant forcing, as would be anticipated from coastal-trapped wave theory.

## 5. Comparison with observations

### a. Alongshore velocity

In this section, the results summarized above are compared with corresponding quantities computed by Brink et al. (1987) from observations at the CODE-2 moorings, beginning with alongshore velocity. The alongshore velocity gain, coherence, and phase at frequency $\omega = 1.08 \times 10^{-5}$ s$^{-1}$ (6.7-day period) estimated by Brink et al. (1987) are shown in Fig. 9. Over the outer half of the shelf, the gain is nearly independent of depth and decays offshore. Over the inner half of the shelf, the gain has a more complex spatial dependence, as it increases onshore at the surface, but has an interior (subsurface) maximum 5–10 km offshore. Both the qualitative spatial structure and the magnitude of the observed gains are reproduced by the linear model (Figs. 2a,b). The offshore interior maximum is found in both the observations (Fig. 10) and the model (Fig. 2b) throughout the range of frequencies considered and decreases with frequency in both.
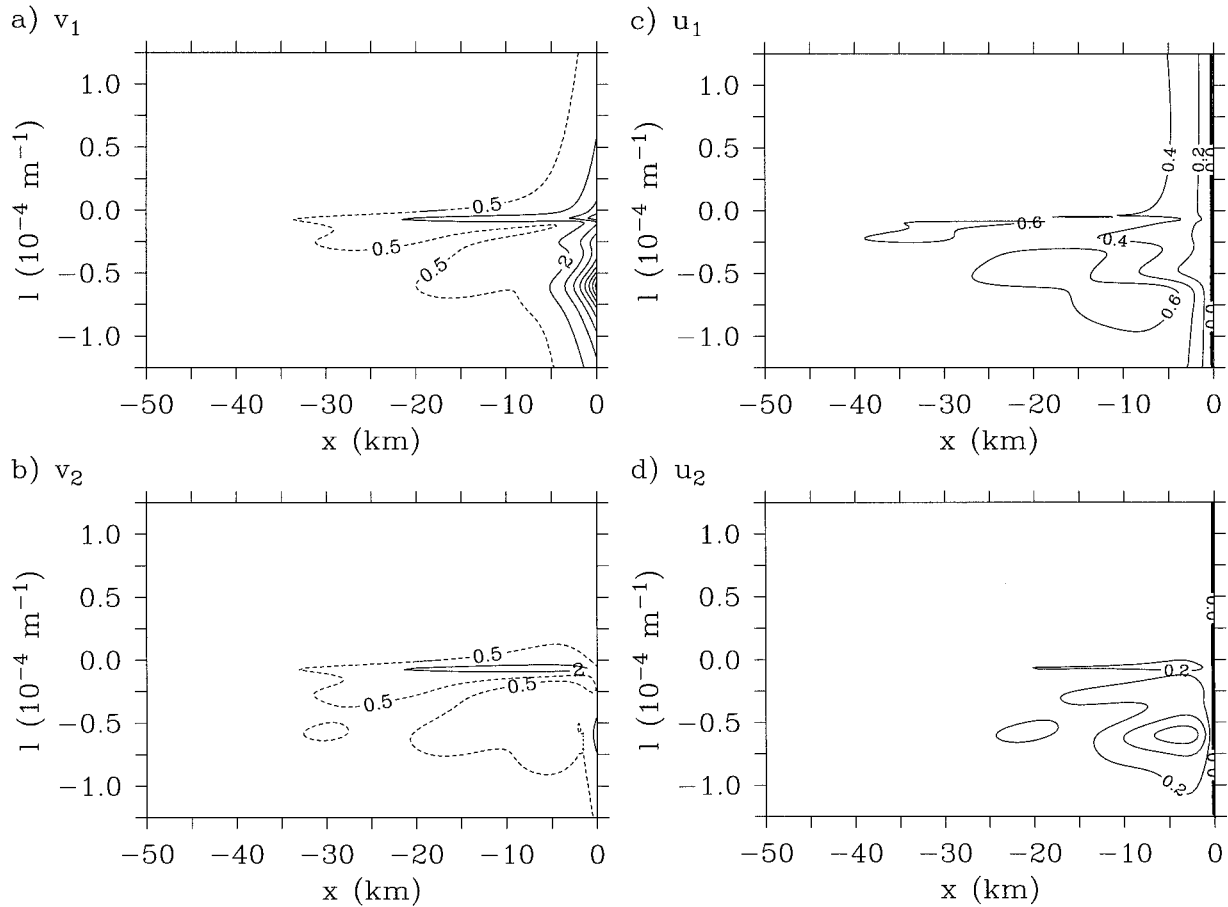
FIG. 7. Contours of transfer function amplitude $(B_x \overline{B}_x)^{1/2}$ for variable $X$ at frequency $\omega = 1.08 \times 10^{-5}$ s$^{-1}$ vs cross-shore distance $x$ and alongshore wavenumber $l$: $X =$ (a) $v_1$, (b) $v_2$, (c) $u_1$, (d) $u_2$, and (e) $\zeta$.

This qualitative and approximate quantitative agreement suggests an explanation of the alongshore interior velocity structure over the inner half of the shelf that differs from previous hypotheses advanced by Brink et al. (1987) and by Lopez-Mariscala and Clarke (1993). Those authors find that in model calculations, an offshore interior maximum in alongshore velocity results when the amplitude of the alongshore winds decreases rapidly onshore of mooring C3, consistent with the weak winds observed at the coastal Sea Ranch station. The evidence is not sufficient to rule out either hypothesis, but it should be noted that the cross-shore profile of alongshore wind amplitude between C3 and Sea Ranch was not measured in detail during CODE, so results depending on assumptions about this profile should be viewed with some caution.

The present model reproduces the observed offshore maximum of alongshore interior velocity gain, even in the absence of a cross-shore gradient in the amplitude of the alongshore wind stress. In addition, the present model reproduces the observed onshore maximum of alongshore surface velocity gain. In contrast, in the model calculations of Brink et al. (1987), the offshore

interior maximum appeared only when a cross-shore gradient of alongshore wind stress amplitude was included, while the onshore surface maximum did not appear at all. The critical difference between the two models is evidently the coastal boundary condition. As discussed above, Brink et al. (1987) employ barotropic boundary conditions, which require that the Ekman transport be balanced at the coast by an oppositely directed, depth-independent interior flow, while in the present model the no-normal-flow condition is enforced separately in the upper and lower layers so that the vertical structure of the motion is directly linked to the vertical distribution of the turbulent stress. Thus, in the present model, the vertical motion associated with Ekman divergence at the coast is required to occur within the model domain; the barotropic boundary conditions instead require that the divergence and vertical motion occur outside the model domain, and demand for their accuracy that this vertical motion have negligible influence on the dynamics within the model domain. The present model also idealizes the interior fluid as homogeneous, while the model of Brink et al. (1987) was linearized about a given resting stratification, but this
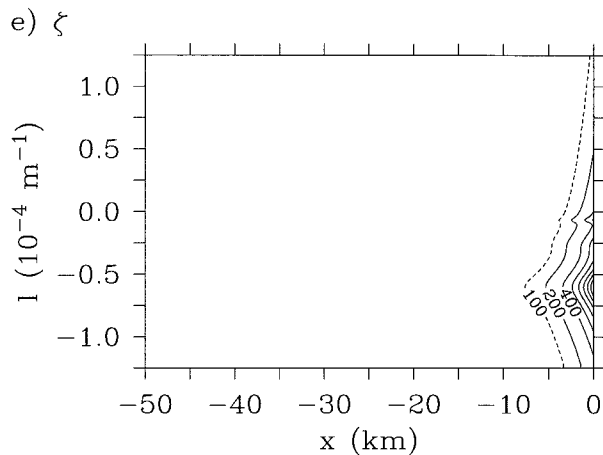
e) $\zeta$



FIG. 7. (*Continued*)



FIG. 9. Contours of alongshore velocity gain $R_vT$ (lower panel) and coherence $\gamma_{vT}$ and phase $\theta_{vT}$ (upper panel) at frequency $\omega = 1.08 \times 10^{-5}$ s$^{-1}$ vs offshore distance and depth, from the CODE C-line moorings. The mooring locations are C2: $x = 2$ km, C3: $x = 5.8$ km, C4: $x = 12.5$ km, and C5: $x = 27.3$ km. The units of gain are cm$^2$ s$^{-2}$/(dyn cm$^{-2}$)$^2$ = 0.1 m$^2$ s$^{-2}$/(N m$^{-2}$)$^2$, so these values should be divided by 10 for comparison with Figs. 2 and 5. (From Brink et al. 1987.)

difference evidently has little influence on the flow over the shelf, as the response of the stratified model was nearly independent of depth over most of the shelf despite the additional baroclinic degrees of freedom.

The predicted (Figs. 3 and 4) and observed (Figs. 9 and 10) alongshore velocity coherence and phase have some similarities, but the agreement is not as striking as for the gain. The offshore decay of model coherence is stronger at the surface than in the interior, but not to the extent observed. As in the observations, there is an offshore interior coherence maximum in the model predictions with a similar decay 10–30 km offshore. The inshore decay of this maximum occurs within 2–3 km of the coast and is more rapid than the observations indicate. The model phase is close to the observed phase over the inner half of the shelf, but the sign of the

offshore trend is wrong. The poor model prediction of offshore phase may be related to the neglect of stratification and to the truncated offshore topographic profile, to frictional effects, or to remote wind forcing. Brink et al. (1987) found a strong dependence of predicted phase on the cross-shore structure of the wind forcing, as well as a dependence of gain and coherence on alongshore gradients of wind stress amplitude.

### b. Cross-shore velocity and temperature

Although the comparison of predicted and observed cross-shore velocity and temperature statistics proves much less successful than for alongshore velocity, it is nonetheless instructive and is briefly summarized here. Unpublished results (D. Chapman 1996, personal communication) of the Brink et al. (1987) statistical analysis of observed cross-shore velocity and temperature from the CODE moorings are summarized in Table 1. The cross-shore velocity statistics have been depth-averaged
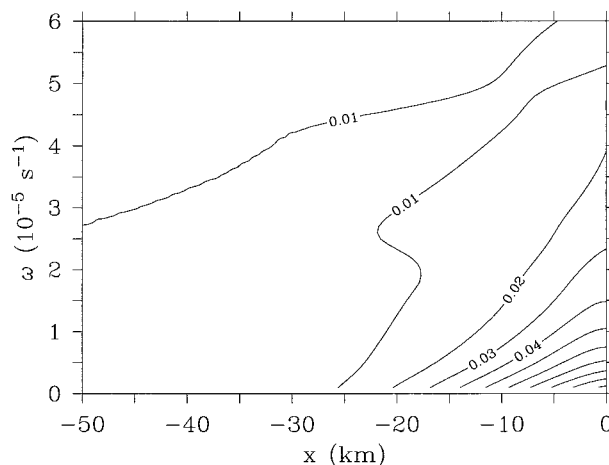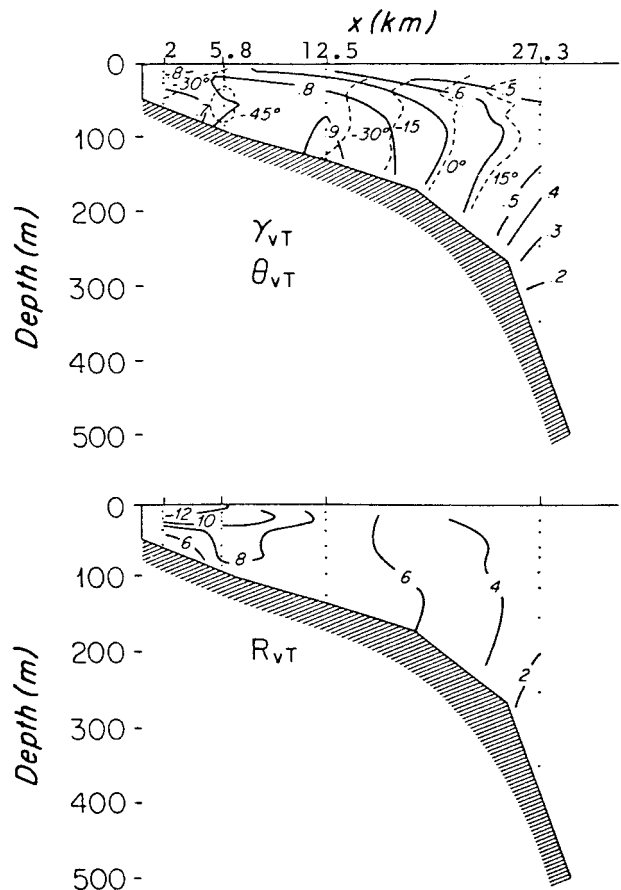


FIG. 8. Contours of inviscid interior lower-layer cross-shore velocity gain vs frequency $\omega$ and offshore distance $x$ for the case with exponential topography and no-normal-flow boundary conditions in each layer. The inviscid interior velocity component is calculated from the full solution as the inertial response to the lower-layer pressure gradient. The gain $R_{u_2T}$ for the full lower-layer cross-shore velocity is shown in Fig. 2d. The units are m$^2$ s$^{-2}$/(N m$^{-2}$)$^2$.
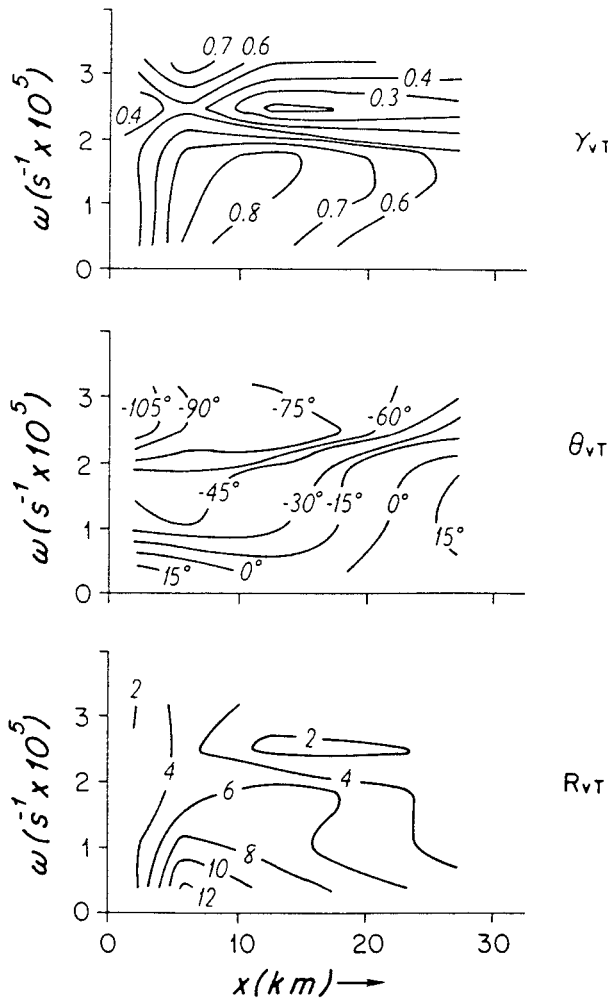
FIG. 10. Contours of alongshore velocity gain $R_v T$ (lower panel), phase $\theta_{vT}$ (middle panel), and coherence $\gamma_{vT}$ (upper panel) at 55-m depth vs offshore distance and frequency from the CODE C-line moorings. The units of gain are cm² s⁻²/(dyn cm⁻²)² = 0.1 m² s⁻²/(N m⁻²)², so these values should be divided by 10 for comparison with the Figs. 2 and 5. (From Brink et al. 1987.)

over the entire domain at all frequencies considered, while the observed coherence above 20 m has an overall maximum value of only 0.82 and tends to weaken offshore and toward higher frequency. Thus, while the predicted wind-driven signal is evident in the observations, the model significantly overpredicts cross-shore velocity coherence in the surface layer. There is a rough correspondence in the magnitudes of the predicted and observed gains, again consistent with wind-driven Ekman dynamics. There is some indication that the model reproduces an observed onshore decrease in gain between moorings C3 and C2, although here the possibility that winds weaken onshore from C3 to C2 complicate the interpretation. The observed alongshore velocity gain (Fig. 9) suggests a tendency of the wind stress to force alongshore flow (rather than cross-shore Ekman transport) as the coastal boundary is approached, which would be consistent with a decrease in cross-shore velocity gain from C3 to C2. The model cross-shore velocity is in phase with the wind in the surface layer, consistent with the observations.

Below 20 m, the observed cross-shore velocity coherences are generally lower, with most average values in the range 0.2–0.5. These relatively small coherences are generally consistent with the demonstration by Dever (1995) that a simple wind-forced two-dimensional model, with a barotropic interior and frictional surface and bottom boundary layers, fails to reproduce observed interior cross-shore velocities at C3 during CODE. Some marginally significant coherences (0.5–0.66) are found at C3 and C4 at the lower frequencies. The marginally significant coherences may be related to minor improvements in the skill of the Dever (1995) model obtained by removing the depth-averaged component of the observed cross-shelf flow and to the weak indication of cross-shore return flow at middepth from the linear statistical model of Davis and Bogden (1987).

The model lower-layer cross-shore velocity coherence is roughly twice as large as the observed coherence, reaching 0.9 near the coastal boundary and decreasing offshore to less than 0.4, roughly independent of frequency except at the highest frequencies. Despite this difference, the model gain is comparable to the observed gain below 20 m over inner half of the shelf. A more complete examination of the data confirms that the ratios of interior cross-shore velocity and wind-stress spectral amplitudes in the model are often within a factor of 2 of the observed ratios over the inshore half of the shelf ($-15$ km $< x < 0$), while the observed ratios are several times larger over the outer half of the shelf. The model gain decreases farther offshore, while the observed gain appears to increase offshore monotonically, though the offshore values have low statistical significance. Since the observed coherences are also small over the outer shelf, it would appear to be consistent to assume that the additional variance is not wind driven. This conclusion would be supported by the more recent observations of Largier et al. (1993), but other explanations

separately above and below 20 m, for comparison with the present results, while the temperature statistics have been averaged over all depths. Average gain and phase were computed only from those records with significantly nonzero coherence. Averaged coherences contain all the coherence values.

The cross-shore velocity statistics above 20 m essentially represent a crude, frequency-dependent test of Ekman dynamics. Lentz (1994) and Dever (1995) have shown that the wind-driven, cross-shore transport in the surface boundary layer at CODE mooring C3 agrees well with the expected Ekman transport, with a substantial fraction being carried in a transition layer beneath a surface mixed layer 0–20 m thick. This is reflected in the high coherences (0.6–0.8) found in this analysis at the lower frequencies. The model surface-layer cross-shore velocity coherence is greater than 0.99

TABLE 1. Coherence, gain, and phase for cross-shore velocity $u$ and temperature $T$ vs alongshore wind stress $\tau$ from C-line CODE-2 observations at periods 454, 161, 98, 70, 55 h (frequencies 0.38, 1.08, 1.78, 2.49, 3.17 $\times 10^{-5}$ s$^{-1}$). I. $u$ (upper 20 m) vs $\tau$, II. $u$ (below 20 m) vs $\tau$, III. $T$ (all depths) vs $\tau$. (a) Average coherence for all records. (b) (number of records with significant coherences/total number of records, average gain, average phase). In (b) average gain and phase are calculated only from those records with significantly nonzero coherence. (Values of gain are in cgs units, as in Figs. 9 and 10.)

**I. $u$ (upper 20 m) vs $\tau$**

a)

|  | C2 | C3 | C4 | C5 |
|---|---|---|---|---|
| 454 h | 0.61 | 0.82 | 0.74 | 0.19 |
| 161 h | 0.71 | 0.47 | 0.08 | 0.36 |
| 98 h | 0.60 | 0.65 | 0.63 | 0.57 |
| 70 h | 0.42 | 0.20 | 0.30 | 0.51 |
| 55 h | 0.47 | 0.36 | 0.24 | 0.49 |

b)

|  | C2 | C3 | C4 | C5 |
|---|---|---|---|---|
| 454 h | (2/2,1.90,12) | (4/4,5.58,0) | (2/2,4.74,−73) | (0/1,—,—) |
| 161 h | (2/2,2.18,−8) | (1/4,4.30,16) | (0/2,—,—) | (0/1,—,—) |
| 98 h | (2/2,1.58,−33) | (4/4,3.46,−2) | (2/2,4.80,11) | (1/1,4.29,42) |
| 70 h | (0/2,—,—) | (0/4,—,—) | (0/2,—,—) | (0/1,—,—) |
| 55 h | (1/2,2.23,−28) | (0/4,—,—) | (0/2,—,—) | (0/1,—,—) |

**II. $u$ (below 20 m) vs $\tau$**

a)

|  | C2 | C3 | C4 | C5 |
|---|---|---|---|---|
| 454 h | 0.26 | 0.52 | 0.62 | 0.18 |
| 161 h | 0.54 | 0.66 | 0.49 | 0.26 |
| 98 h | 0.50 | 0.37 | 0.32 | 0.28 |
| 70 h | 0.32 | 0.47 | 0.48 | 0.40 |
| 55 h | 0.33 | 0.41 | 0.22 | 0.29 |

b)

|  | C2 | C3 | C4 | C5 |
|---|---|---|---|---|
| 454 h | (0/2,—,—) | (2/4,1.93,−24) | (5/5,2.11,−86) | (0/8,—,—) |
| 161 h | (1/2,1.33,−79) | (3/4,1.51,160) | (2/5,2.18,176) | (0/8,—,—) |
| 98 h | (1/2,0.51,−160) | (0/4,—,—) | (0/5,—,—) | (1/8,3.96,25) |
| 70 h | (1/2,0.91,150) | (0/4,—,—) | (3/5,4.33,167) | (0/8,—,—) |
| 55 h | (0/2,—,—) | (1/4,1.45,−111) | (0/5,—,—) | (1/8,5.55,−76) |

**III. $T$ (all depths) vs $\tau$**

a)

|  | C2 | C3 | C4 | C5 |
|---|---|---|---|---|
| 454 h | 0.84 | 0.74 | 0.59 | 0.43 |
| 161 h | 0.76 | 0.66 | 0.54 | 0.48 |
| 98 h | 0.40 | 0.41 | 0.24 | 0.51 |
| 70 h | 0.17 | 0.30 | 0.29 | 0.30 |
| 55 h | 0.25 | 0.23 | 0.19 | 0.35 |

b)

|  | C2 | C3 | C4 | C5 |
|---|---|---|---|---|
| 454 h | (4/4,0.78,−40) | (8/8,0.65,−54) | (5/7,0.50,−73) | (1/9,0.22,−102) |
| 161 h | (4/4,0.29,−76) | (7/8,0.23,−96) | (4/7,0.17,−96) | (3/9,0.12,−40) |
| 98 h | (1/4,0.18,−93) | (2/8,0.14,−78) | (1/7,0.07,−165) | (5/9,0.09,−76) |
| 70 h | (0/4,—,—) | (0/8,—,—) | (0/7,—,—) | (1/9,0.13,−119) |
| 55 h | (/4,—,—) | (0/8,—,—) | (0/7,—,—) | (1/9,0.09,−79) |

(such as remote wind driving, which can reduce coherence with local forcing) are also possible. The model cross-shore velocity is out of phase with the wind in the interior, generally consistent with observations below 20 m with some exceptions, most notably at the lowest frequency.

The lower-layer cross-shore velocity statistics from the present model thus appear to compare better with observations than did the model results of Brink et al. (1987), for which the predicted cross-shore velocities were more than an order of magnitude smaller than observations. However, the present model combines both the interior and bottom boundary-layer flow. Since the enhanced cross-shore flow in the present model is

frictionally driven (Fig. 8), it is probably appropriate to interpret this as bottom boundary-layer transport, which was excluded from the cross-shore velocities by Brink et al. (1987). Although observations indicate the presence of a bottom boundary layer with substantial cross-shore transport (Dever 1995), it is more difficult to determine directly the degree to which the interior flow over the inner half of the shelf is inviscid. For example, Davis and Bogden (1989) find a significant departure from geostrophy throughout the water column as far offshore as the 60-m isobath, which they interpret as evidence of turbulent stresses penetrating the entire water column at that depth. The coastal boundary conditions indirectly affect the structure of the cross-shore

velocity response since the cross-shore velocity is driven primarily by the bottom stress from the alongshore flow, whose cross-shore structure is in turn affected by the coastal boundary conditions. Thus, it is possible that the distribution of the cross-shore velocity response between interior and bottom boundary layer could also be affected by the coastal boundary condition.

Two conclusions may be drawn from this comparison. First, the predicted cross-shore velocities, which are evidently dominated by the return flow that balances the surface Ekman transport, are smaller than, but of the same order of magnitude as, the observed cross-shore velocities. Presumably, Brink et al. (1987) would have found a similar result if they had included the bottom Ekman layer flow in their predicted cross-shore velocities. Second, although important questions remain concerning the depth distribution of the observed return flow and its partition between frictional and inviscid dynamics, it seems likely that the rough agreement between predicted and observed cross-shore velocity gains is fortuitous and indicates only that the observed interior cross-shore velocity variance happens to be of the same order of magnitude as the lower-layer return flow in the model, which should more properly be confined to a bottom Ekman layer rather than being distributed over the interior.

The comparison of the statistics of model interface displacement and observed temperature fluctuations is difficult because of the crude representation of vertical structure by the two-layer model. The model coherence (Fig. 2e), with an approximately linear offshore decay, is consistent with the observed coherences at the two lowest frequencies, but the model coherences are much higher than observed at the higher frequencies. Rough correspondence of model and observed gains over the central shelf could be achieved by converting interface displacement to temperature fluctuations using a surface-layer base vertical gradient of 2.5°C/5 m, but this seems unreasonably sharp relative to observed vertical structure. Adjacent to the coastal boundary, where the model interface displacements are much greater, the model does generate effective temperature fluctuations comparable to those observed over the central shelf. Thus, the model interface displacements do not appear to be sufficient to explain the observed temperature fluctuations over the central shelf, while displacements near the coastal boundary would be sufficient, but do not extend far enough offshore. Thus, the absence of horizontal temperature advection in the model is a likely cause of this discrepancy.

*c. Related observational results*

A variety of frequency-dependent response functions have been computed from the CODE data. The focus of the present comparison has been on those computed by Brink et al. (1987), since they may be compared to the present model predictions in a relatively straight-

forward manner. Two other analyses of relevance here are the frequency-dependent empirical orthogonal function analysis of Denbo and Allen (1987), and the linear statistical model responses computed by Davis and Bogden (1987). Brief reference to the latter has been made above.

Denbo and Allen (1987) show that the highest spatial-lagged coherences (≥0.7) in the 2–10 day period band between alongshore wind stress and alongshore currents at CODE mooring C5 during 1982 are found for wind stress 100–350 km to the south of the mooring. These coherences are significantly larger than those computed by Brink et al. (1987) between local winds and currents at C5 (Figs. 9 and 10), consistent with the hypothesis that much of the alongshore velocity variability at C5 is associated with remote forcing.

Davis and Bogden (1987) compute the vector velocity response to alongshore winds in the 4–12 day period band using a linear statistical model. The response is dominated by depth-independent alongshore flow, but the component in phase with the winds has significant vertical shear and cross-shore flow. The tendency of the vertical shear in the cross-shore flow is generally consistent with flow in surface and bottom Ekman layers. Over the central shelf, the linear model explains more than half of the alongshore flow, but a smaller fraction of cross-shore flow: roughly half near the surface and bottom, and only a third at middepth. Similar results were obtained in the 2.5–4 day period band, with a stronger cross-shore surface flow and a cross-shore return flow below that varied less with depth. A significant departure from geostrophy in the alongshore flow component was found throughout the water column at the 60-m isobath. These results appear to be consistent with the hypothesis that some of the cross-shore return flow at these frequencies may occur above the bottom boundary layer, though the evidence is far from conclusive.

## 6. Summary

The present results suggest that useful insight into the dynamics of wind-forced currents over the inner half of the shelf in the CODE region may be gained from an idealized two-layer model in which the upper layer (of order 20-m depth) represents a surface wind-mixed layer and the lower layer contains both the inviscid interior and the bottom boundary layer.

For periods of 2–7 days, the model credibly reproduces some aspects of the statistical analysis of CODE observations reported by Brink et al. (1987). The structure and magnitude of the alongshore velocity gain over the inner half of the shelf (within 15 km of the coast) are reproduced in considerable detail by the present model, particularly at the lower frequencies. An onshore maximum in near-surface alongshore velocity gain and an offshore maximum in interior alongshore velocity gain are predicted, which do not depend on cross-shore gradients of the alongshore wind stress or the bottom friction coef-

ficient. The cross-shore velocity response is reproduced to some degree, but the agreement with observational estimates degrades rapidly toward the slope, as the predicted variances are too small. Since observed coherences were small over the slope, this discrepancy could be rationalized by the assumption that the cross-shore velocity variance over the slope is not primarily forced by local winds. Although the model reproduces the amplitude of cross-shore velocities over the inner half of the shelf within roughly a factor of 2 and transfer functions do indicate an enhancement of the lower-layer cross-shore velocity response associated with the baroclinic modifications of the resonant shelf wave, this agreement is probably misleading because the model lower-layer cross-shore velocities are dominated by the frictionally driven flow, which is included in the lower layer flow rather than being confined to a bottom Ekman layer. Thus, it may simply indicate that the additional (unpredicted) cross-shore flow is comparable in magnitude to the bottom Ekman flow. The observed temperature fluctuations over the central shelf are not reproduced by the model, but the energetic model interface displacements adjacent to the coastal boundary appear to be comparable to observed temperature fluctuations. The absence of horizontal temperature advection is a likely cause of the discrepancy over the central shelf.

The agreement of observed and predicted vertical and cross-shore structure of the alongshore velocity gain over the inner half of the shelf suggests that this structure may result from a reduced Ekman transport response and an enhanced alongshore flow acceleration response to the alongshore wind stress over the inner half of the shelf. This differs from the hypothesis advanced by Brink et al. (1987) and Lopez-Mariscala and Clarke (1989), who show that an offshore maximum in alongshore interior velocity gain can result from a rapid onshore decrease in the magnitude of the wind stress.

The main physical difference between the present and previous related models is that, in the present model, the interior interface at the coast is allowed to move vertically in response to wind-forced divergence associated with the no-normal-flow condition at the coastal boundary. This contrasts with models based on coastal-trapped wave theory in which the corresponding vertical motion is presumed to occur in the inner shelf and nearshore regimes, outside the model domain, and a baroclinic response at the coastal boundary is explicitly prevented by the barotropic form of the boundary conditions. In the present model, the differences in boundary condition are primarily felt in a baroclinic zone adjacent to the coast whose width is set by the local internal deformation radius at the outer edge of the stagnant inner shelf. For the CODE observations in the period band 2–7 days, the present results suggest that a similar baroclinic adjustment zone evidently exists over a significant portion of the shelf. In general, the dependence of the interior flow over the inner half of the shelf on the details of the coastal boundary condition is unset-tling, given the idealized nature of these conditions. It points to the need for improved understanding of the dynamics that control horizontal divergence and vertical motion in the inner shelf and nearshore regimes.

## REFERENCES

Allen, J., 1975. Coastal trapped waves in a stratified ocean. *J. Phys. Oceanogr.,* **5,** 300–325.
——, 1980 Models of wind-driven currents on the continental shelf. *Annu. Rev. Fluid Mech.,* **12,** 389–433.
——, and D. Denbo, 1984. Statistical characteristics of the large-scale response of coastal sea level to atmospheric forcing. *J. Phys. Oceanogr.,* **14,** 1079–1094.
——, P. Newberger, and J. Federiuk, 1995. Upwelling circulation on the Oregon continental shelf. Part I: Response to idealized forcing. *J. Phys. Oceanogr.,* **25,** 1843–1866.
Battisti, D., and B. Hickey, 1984. Application of remote wind-forced coastal trapped wave theory to the Oregon and Washington coasts. *J. Phys. Oceanogr.,* **14,** 887–903.
Brink, K., 1982. A comparison of long coastal trapped wave theory with observations off Peru. *J. Phys. Oceanogr.,* **12,** 897–913.
——, 1989. Energy conservation in coastal-trapped wave calculations. *J. Phys. Oceanogr.,* **19,** 1011–1016.
——, 1991. Coastal-trapped waves and wind-driven currents over the continental shelf. *Annu. Rev. Fluid Mech.,* **23,** 389–412.
——, D. Chapman, and G. Halliwell Jr., 1987. A stochastic model for wind-driven currents over the continental shelf. *J. Geophys. Res.,* **92,** 1783–1797.
Chapman, D., 1987. Application of wind-forced, long, coastal-trapped wave theory along the California coast. *J. Geophys. Res.,* **92,** 1798–1816.
Church, J., N. White, A. Clarke, H. Freeland, and R. Smith, 1986. Coastal-trapped waves on the east Australian continental shelf. Part II: Model verification. *J. Phys. Oceanogr.,* **16,** 1945–1957.
Clarke, A., and M. Lopez, 1987. The influence of sloping mean density surfaces on low-frequency shelf water flow. *J. Phys. Oceanogr.,* **17,** 507–517.
Davis, R., and P. Bogden, 1989. Variability on the California shelf forced by local and remote winds during the Coastal Ocean Dynamics Experiment. *J. Geophys. Res.,* **94,** 4763–4783.
Denbo, D., and J. Allen, 1987. Large-scale response to atmospheric forcing of shelf currents and coastal sea level off the west coast of North America: May–July 1981 and 1982. *J. Geophys. Res.,* **92,** 1757–1782.
de Szoeke, R., and J. Richman, 1984. On wind-driven mixed layers with strong horizontal gradients—A theory with application to coastal upwelling. *J. Phys. Oceanogr.,* **14,** 364–377.
Dever, E., 1995. Subtidal cross-shelf circulation on the northern California shelf. Ph.D. thesis, MIT/WHOI Joint Program 95-16, 162 pp.
Federiuk, J., and J. Allen, 1995. Upwelling circulation on the Oregon continental shelf. Part II: Simulations and comparisons with observations. *J. Phys. Oceanogr.,* **25,** 1867–1889.
Gill A., and E. Schumann, 1974: The generation of long shelf waves by the wind. *J. Phys. Oceanogr.,* **4,** 83–90.
Huthnance, J., 1975. On trapped waves over a continental shelf. *J. Fluid Mech.,* **69,** 689–704.

Largier, J., B. Magnell, and C. Winant, 1993. Subtidal circulation over the northern California shelf. *J. Geophys. Res.,* **98,** 18 147–18 179.

Lentz, S., 1992. The surface boundary layer in coastal upwelling regions. *J. Phys. Oceanogr.,* **22,** 1517–1539.

——, 1994. Current dynamics over the northern California inner shelf. *J. Phys. Oceanogr.,* **24,** 2461–2478.

Lopez, M., and A. Clarke, 1989. The wind-driven shelf and slope water flow in terms of a local and remote response. *J. Phys. Oceanogr.,* **19,** 1092–1101.

Lopez-Mariscala, M., and A. Clarke, 1993. On the influence of wind-stress curl on low-frequency shelf water flow. *J. Phys. Oceanogr.,* **23,** 2717–2727.

Mitchum, G., and A. Clarke, 1986. The frictional nearshore response to forcing by synoptic scale winds. *J. Phys. Oceanogr.,* **16,** 934–946.

Samelson, R., and R. de Szoeke, 1988. Semigeostrophic wind-driven thermocline upwelling at a coastal boundary. *J. Phys. Oceanogr.,* **18,** 1372–1383.

Winant, C., R. Beardsley, and R. Davis, 1987. Moored wind, temperature, and current observations made during Coastal Ocean Dynamics Experiments 1 and 2. *J. Geophys. Res.,* **92,** 1569–1604.